Nanoscale

PAPER

View Article Online
View Journal | View Issue

Cite this: *Nanoscale*, 2018, **10**, 3849

Evolution of surface catalytic sites on thermochemically-tuned gold–palladium nanoalloys†

Haval Kareem,[a] Shiyao Shan,[a] Fang Lin,[a] Jing Li,[a] Zhipeng Wu,[a] Binay Prasai,[b] Casey P. O'Brien,[c] Ivan C. Lee,*[c] Dat T. Tran,[c] Lefu Yang,[d] Derrick Mott,[e] Jin Luo,[a] Valeri Petkov *[b] and Chuan-Jian Zhong *[a]

Received 23rd November 2017,
Accepted 20th January 2018

DOI: 10.1039/c7nr08748a

rsc.li/nanoscale

Nanoscale alloying constitutes an increasingly-important pathway for design of catalysts for a wide range of technologically important reactions. A key challenge is the ability to control the surface catalytic sites in terms of the alloying composition, thermochemical treatment and phase in correlation with the catalytic properties. Herein we show novel findings of the nanoscale evolution of surface catalytic sites on thermochemically-tuned gold–palladium nanoalloys by probing CO adsorption and oxidation using *in situ* diffuse reflectance infrared Fourier transform spectroscopy (DRIFTS) technique. In addition to the bimetallic composition and the support, the surface sites are shown to depend strongly on the thermochemical treatment condition, demonstrating that the ratio of three-fold *vs.* bridge or atop Pd sites is greatly reduced by thermochemical treatment under hydrogen in comparison with that under oxygen. This type of surface reconstruction is further supported by synchrotron high-energy X-ray diffraction coupled to atomic pair distribution function (HE-XRD/PDF) analysis of the nanoalloy structure, revealing an enhanced degree of random alloying for the catalysts thermochemically treated under hydrogen. The nanoscale alloying and surface site evolution characteristics were found to correlate strongly with the catalytic activity of CO oxidation. These findings have significant implications for the nanoalloy-based design of catalytic synergy.

1. Introduction

Carbon monoxide (CO), a highly toxic gas produced from combustion of fossil fuels, has negative effects on human health and leads to symptoms of various diseases depending on the exposure concentration and duration.[1,2] Hydrogen, produced from natural gases for use in fuel cells, often contains traces of CO which could poison the catalysts. Catalytic oxidation is essential in converting CO into non-toxic or non-poisonous species.[3] The need for finding effective ways to remove chemical pollutants and harmful gases such as CO and other toxic gases is an important driving force for the research and development of highly effective catalysts. Catalysts derived from noble metals such as palladium and platinum have sparked attentions of many researchers due to their high catalytic activities for CO oxidation.[4,5] However, the high cost of noble metals is a major concern to practical application. Alloying palladium with non-noble metal is an important pathway to reduce the cost. Importantly, it could enhance the catalyst's activity in many reactions. Addition of second or third metals (*e.g.*, Au, Ni, Co, *etc.*) can have magnificent promotional effect on the catalytic activity as compared to the constituent monometallic palladium catalyst.[6] While alloying Pd with different base transition metals has been considered in many reactions including CO oxidation,[7] the stability constitutes a major challenge due to their different oxidation potentials. AuPd, as a stable catalyst, has been largely used in direct synthesis of hydrogen peroxide from H_2 and O_2,[8] and the oxidation of primary alcohols to aldehydes.[9]

The choice of support is also an important consideration in the development of nanocatalysts because the interaction of

[a]*Department of Chemistry, State University of New York at Binghamton, Binghamton, NY 13902, USA. E-mail: cjzhong@binghamton.edu*
[b]*Department of Physics, Central Michigan University, Mt. Pleasant, Michigan 48859, USA. E-mail: petko1vg@cmich.edu*
[c]*U.S. Army Research Laboratory, Sensors and Electron Devices Directorate, Adelphi, MD 20783, USA. E-mail: ivan.c.lee2.civ@mail.mil*
[d]*College of Chemistry and Chemical Engineering, Xiamen University, Xiamen 361005, China*
[e]*School of Materials Science, Japan Advanced Institute of Science and Technology, Nomi, Ishikawa 923-1292, Japan*

†Electronic supplementary information (ESI) available: Additional TEM data, catalytic activity data (Fig. S1–S5; Tables S1 and S2), and DRIFTS data (Fig. S6–S9). See DOI: 10.1039/c7nr08748a

nanoparticles with support has a profound effect on the catalytic activity. The interaction influences the specific atomic configuration and atomic strain.[10] Reducible supports such as CeO_2 or TiO_2 also provide an excellent source of oxygen. In a recent study[11] of AuPd on ceria–zirconia prepared by precipitation of Au and incipient wetness impregnation of Pd, CO conversion was found to depend on type of metal support and dispersion. The catalyst with 10 : 1 Au to Pd ratio was found to be optimal. In an earlier study of titania (TiO_2)-supported AuPd catalysts from dendrimer-encapsulated nanoparticle precursors, the activity of bimetallic AuPd was found to be higher than that for monometallic Au and Pd, indicating synergistic effect of the bimetallic components and the support.[12] In another study on the enhanced activity of bimetallic AuPd supported on carbon for oxidation of ethylene glycol and 1,2-propanediol in the aqueous phase, AuPd catalysts synthesized by electroless deposition of Au into Pd/C were shown to exhibit higher activity than those of Au and Pd catalysts. The enhanced activity was attributed to weakening of adsorbate binding energy and reduction of the barrier for the rate determining step due to electronic modification and ensemble effect.[13] Such AuPd supported on SiO_2 was also found to be highly active for propylene hydrogenation *via* the prevention of multiple bonding of propylidyne on discontinuous Pd surface sites as a result of Au presence.[14] The catalytic performance of alloyed AuPd for hydrodechlorination of chlorofluorocarbons was also found to show higher activity compared to monometallic Au and Pd.[15] Theoretical studies have also made significant progress recently. For example, in a study of CO oxidation over 55-atom Au–Pd clusters, the adsorption energy on Au atoms was found to be the lowest at 50 : 50 Au : Pd ratio while Au enriched cluster was predicted to be highly active catalytically because of cooperation of structural and electronic effects.[16] The catalytic enhancement of AuPd alloy catalysts as a result of decrease of bonding energy of strongly bonded adsorbates was also supported by computational studies.[13]

The understanding of the catalytic synergy of the AuPd nanoalloy catalysts requires the abilities to determine the surface catalytic sites and the detailed alloying phase structures. To determine the active catalytic sites, DRIFTS (diffuse reflectance infrared Fourier transform spectroscopy) technique is powerful in probing the surface intermediate species through which information on the surface catalytic sites can be extracted,[17] especially during catalytic reactions.[18] For CO adsorption on a metal (M), the so called "σ donation–π back donation" interaction weakens the CO triple bond, leading to downshift of the vibrational stretching band's wavenumber. The detection of the shift and the relative absorbance intensity provides information for assessing the detailed adsorption mode and the surface sites. The addition of Au to Pd increases activity and stability through ligand and ensemble effects. For Pd, ensemble effect involves dilution of Pd atoms on the surface by gold atoms, in which a high percentage of gold on the nanoparticle surface was reported to lead to the formation of isolated monomer, dimer, or trimer palladium sites.[19] Such an isolation of Pd was ascribed for the high activity of AuPd in vinyl acetate synthesis.[20] Surface segregation of Au and Pd was also reported to occur under reaction condition in the presence of CO and O_2. The surface reconstruction on AuPd, leading to decrease in surface active Au sites, was believed to correlate with the strong deactivation for CO oxidation reaction.[21,22]

In these earlier studies, phase segregation of AuPd nanoparticles in the presence of CO was the main characterisitcs. However, little is known about how the bimetallic composition, thermal treatment and support property are operational for AuPd nanoparticles's phase properties in correlation with the catalytic properties. Herein we show new findings demonstrating that AuPd nanocatalysts remain alloyed during CO oxidation reaction which correlates with the bimetallic composition, reaction atmosphere, and support properties. The study stems from the composition tunability of the phase structures of AuPd nanoparticles, and focuses on investigation of the catalytic oxidation of CO in correlation with the nanoscale phase structures provided by synchrotron high-energy X-ray diffraction (HE-XRD) coupled to atomic pair distribution function (PDF) analysis and the surface species during the catalytic reaction provided by *in situ* real-time DRIFTS characterization. HE-XRD/PDF analysis has recently proven powerful in determining the nanoscale phase structures at atomic scale for a number of bimetallic/trimetallic nanoalloy catalysts.[23–25]

2. Experimental section

2.1. Chemicals

Palladium(II) acetylacetonate ($Pd(acac)_2$, 97%), oleylamine ($CH_3(CH_2)_7CH{=}CH(CH_2)_8NH_2$, 70%), and borane–morpholine (95%) were purchased from Aldrich. Hydrogen tetrachloroaurate(III) hydrate ($HAuCl_4{\cdot}xH_2O$, 99.9%) was purchased from Strem Chemicals. Other chemicals such as ethanol, hexane, and isopropanol were purchased from Fisher Scientific. Vulcan carbon XC-72 was obtained from Cabot. Gases of CO (1 vol% balanced by N_2), H_2 (99.99 vol%), N_2 (99.99 vol%) and O_2 (20 vol% balanced by N_2) were obtained from Airgas. All chemicals were used as received. TiO_2 was purchased from Acros organics. Au/TiO_2 was purchased from World Gold Council.

2.2. Synthesis of AuPd nanoparticles

The synthesis of AuPd nanoparticles of different compositions involved the reduction reaction of two metal precursors.[26] Briefly, $HAuCl_4{\cdot}xH_2O$ and palladium(II) acetylacetonate were dissolved in a desired molar ratio into 15.0 ml oleylamine in a glass vial by heated up to 40 °C with 1.9 mmol borane morpholine at 75 °C under N_2 atmosphere. The resulted solution was then heated up to 220 °C and kept for 30 minutes before cooling down to 70 °C. The NPs were first precipitated out by adding 40 mL isopropanol for centrifugation at 3000 rpm for 20 min and then re-dissolved in 15 mL hexane and 35 ml ethanol mixture cleaning solvent for centrifugation at 3000 rpm for 30 min. The NPs were redispersed in hexane solvent for further use. Note that the particle sizes varied due to subtle

differences in the actual reaction temperature, which led to subtle differences in the bimetallic composition for nanoparticles synthesized under the same feeding ratio.

2.3. Catalysts preparation

The catalysts were prepared from these as-synthesized nanoparticles, including assembling, and thermal activation. Carbon black XC-72, and TiO_2 powder were used as support materials which were mixed with controlled amount of as synthesized nanoparticles followed by sonication and overnight stirring. The product powder was collected and dried under N_2. Carbon- and TiO_2-supported nanoparticles were activated by thermochemical processing, details of which were reported previously.[27] Typically, the supported nanoparticles were first treated at 120 °C under N_2 to remove the organic solvent. It was followed by heating at 260 °C under 20% O_2 (balanced by 80% N_2) for 1 h for removing the organic capping molecules, and then to 400 °C under 15% H_2/85% N_2 for 2 hours for calcining the catalysts. The weight loadings of the carbon supported AuPd/C and for AuPd/TiO_2 were around 15% for most of the catalysts studied in this work.

2.4. Catalytic activity measurement

To measure the catalytic activity of supported AuPd catalysts for CO (1 vol% balanced by N_2) + O_2 (20 vol% balanced by N_2) reaction, a custom-built system was employed, including a temperature-controlled reactor, gas flow/mixing/injection controllers, and an on-line gas chromatograph (Shimadzu GC 8A) equipped with 5A molecular sieve and Porapak Q packed columns and a thermal conductivity detector. The catalysts were loaded in a quartz micro-reactor tube (inner diameter: 4 mm) and wrapped by quartz wool in the middle of the tube (length of the catalyst bed: 6 mm). At a flow rate of 20 ml min^{-1}, the system was injected with the feeding gas (0.5 vol% CO + 10 vol% O_2 balanced by N_2) through the mounted catalyst bed in the quartz micro reactor The residence time was about 0.2 seconds. Gas hourly space velocity (GHSV) in our system is around 16 000 h^{-1}. Temperature control was achieved by a furnace and ice sheath coupled with a temperature controller. The performance of the catalysts of CO oxidation were determined by analysis of composition of the tail gas effusing from the quartz micro reactor packed with the catalyst fixed bed by the on-line gas chromatograph.

2.5. Morphology and composition characterization

Transmission Electron Microscope (TEM) was used to determine the size of nanoparticle. The nanoparticle samples were suspended in hexane solution and were drop cast onto a carbon-coated copper grid followed by solvent evaporation in ambient atmosphere at room temperature.

2.6. High-angle annular dark-field scanning transmission electron microscopy (HAADF-STEM)–energy dispersive spectroscopy (EDS)

HAADF-STEM–EDS was utilized to determine the morphology and map of elemental distribution of the nanoparticles. Following suspension of the sample in hexane solution, then the nanoparticles were drop cast onto carbon-coated copper grid. The measurements were performed on JEOL-ARM200F instrument with an acceleration voltage of 200 kV.

2.7. Inductively coupled plasma – optical emission spectroscopy (ICP-OES)

ICP-OES was employed to examine the composition. It was done on a PerkinElmer 2000 DV ICP-OES instrument using a cross flow nebulizer with the following parameters: plasma 18.0 L $Ar_{(g)}$ min^{-1}; auxiliary 0.3 L $Ar_{(g)}$ min^{-1}; nebulizer 0.73 L $Ar_{(g)}$ min^{-1}; power 1500 W; peristaltic pump rate 1.40 mL min^{-1}. Elements < 1.0 mg L^{-1} were analyzed using a Meinhardt nebulizer attached to a cyclonic spray chamber to rise analyte sensitivity with the following parameters: 18.0 L $Ar_{(g)}$ min^{-1}; auxiliary 0.3 L $Ar_{(g)}$ min^{-1}; nebulizer 0.63 L $Ar_{(g)}$ min^{-1}; power 1500 W; peristaltic pump rate 1.00 mL min^{-1}.

2.8. Diffuse reflectance infrared fourier transform spectroscopy (DRIFTS)

DRIFTS measurement was performed to characterize the surface CO adsorption sites on a Bruker Vertex 70 FTIR spectrometer with a MCT detector and a Praying Mantis™ Diffuse Reflectance Accessory (Harrick Scientific Products, Inc.). Briefly, the sample cup in Praying Mantis™ Diffuse Reflectance Accessory was filled up with 30 mg AuPd/TiO_2 catalysts for the CO adsorption and CO oxidation reaction analysis. The catalysts were pre-treated following the protocol: (1) first at 260 °C for 30 min under O_2 atmosphere; and (2) then at 400 °C for 30 min under H_2 atmosphere.

2.9. Synchrotron high-energy XRD (HE-XRD)

Ex situ HE-XRD measurements were carried out both on in-house equipment and using synchrotron radiation X-rays (E = 80.725 keV) at the beamline 1-ID at the Advanced Photon Source at the Argonne National Laboratory. The XRD diffraction data were reduced to the so-called structure factors, $S(q)$, and then Fourier transformed to atomic PDFs $G(r)$. High-energy XRD and atomic PDFs have already proven to be very efficient in studying the atomic-scale structure of nanosized materials,[28,29] including AuPd NPs.[34]

2.10. Computational modeling

Ab initio calculations were conducted by DFT with DMol^3 program (a part of Materials Studio). In the computation, the generalized gradient approximation (GGA) were used. Minimization of energy of all model atomic configuration for unsupported AuPd clusters were carried out. To interrogate the interaction between CO molecule and the model atomic configurations, the energy of adsorption of CO on the model atomic configurations was calculated by $E_{ads} = -(E_{CO-metal} - E_{metal} - E_{CO})$, where, $E_{CO-metal}$, E_{metal} and E_{CO} are total energy for the CO–metal complex, the isolated metal cluster, and the isolated CO molecule, respectively.

3. Results and discussion

Fig. 1A and B show a representative set of HAADF-STEM imaging and EDS mapping data for a sample of $Au_{45}Pd_{55}/TiO_2$. It is evident that the nanoparticles feature bimetallic composition. The lattice fringe determined from the AuPd (111) is 0.230 nm, which falls in between Pd and Au NPs, 0.225 and 0.236 nm, respectively,[30,31] indicative of alloy characteristic. The bulk compositions of the AuPd nanoparticles of several different bimetallic compositions were analyzed using ICP-OES method. Fig. 1C shows a representative plot of Au% in these nanoparticles and the feeding composition in their synthesis solution. In comparison with a 1 : 1 linear relationship between the feeding and nanoparticle compositions, Pd is shown to be slightly more favorable in the bimetallic nanoparticles than Au under the synthesis condition. Because of the metal selectivity in the NPs, the feeding ratios in $Au_{25}Pd_{75}$, $Au_{50}Pd_{50}$, and $Au_{75}Pd_{25}$ were found to form NPs with subtle differences in composition, Au_9Pd_{91}, $Au_{45}Pd_{55}$, and $Au_{69}Pd_{31}$. Bimetallic composition is often influenced by the size of the resulting nanoparticles,[32] and the synthesis reaction temperature. Indeed, the NPs featured an average particle size of 6.5 ± 0.6 nm, 3.7 ± 0.4 nm 5.5 ± 0.8 nm and 5.3 ± 0.9 nm for Au_9Pd_{91}, $Au_{21}Pd_{79}$, $Au_{45}Pd_{55}$, and $Au_{69}Pd_{31}$, respectively. Note that the particle sizes for Au_9Pd_{91} and $Au_{21}Pd_{79}$ were quite different (Fig. S1†) due to subtle difference in the reaction temperature, as indicated in the Experimental section. Larger sized particles were also found to be richer in Pd than that of the smaller-sized particles in a previous study.[33] For the chemical pattern for AuPd NPs supported on carbon, we have recently shown[34] that the composition map for $Au_{45}Pd_{55}$ and $Au_{69}Pd_{31}$ indicates a near homogeneous nanoalloy. However, the map of Au_9Pd_{91} shows that Au atoms tend to segregate toward nanoparticle surface,

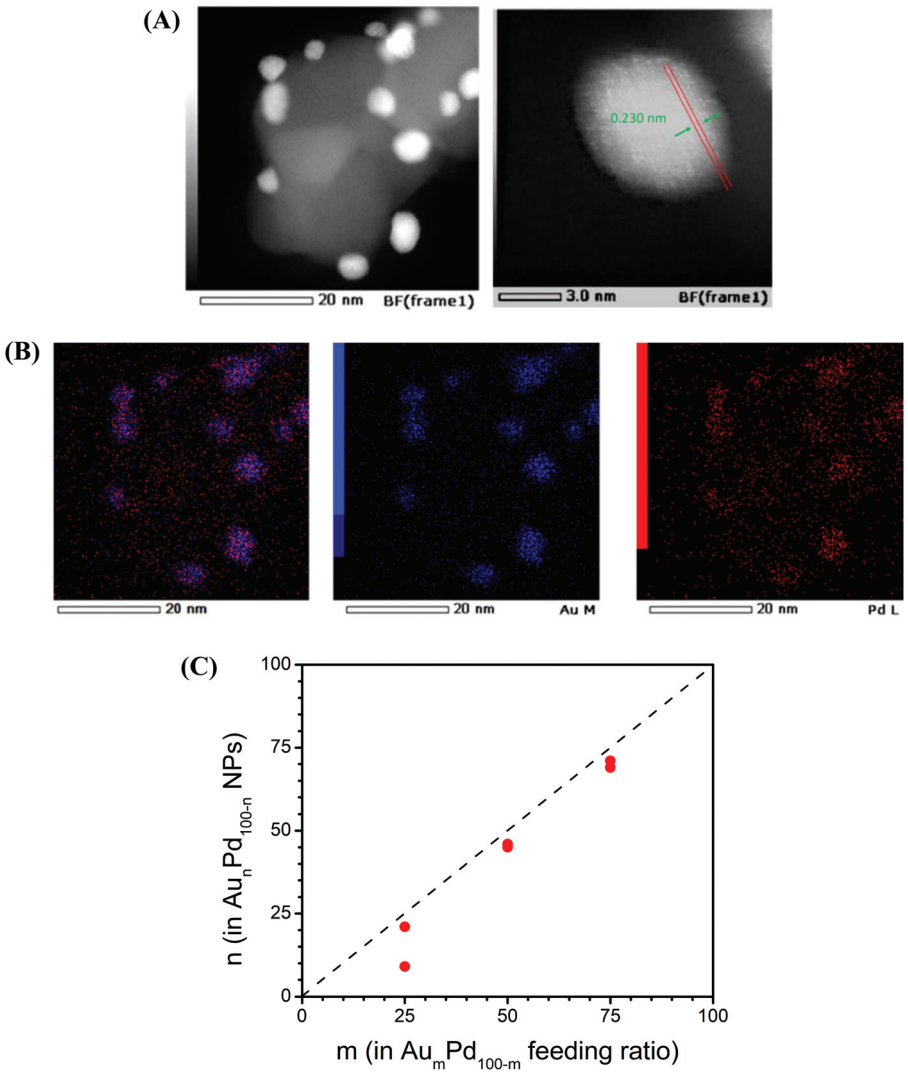

Fig. 1 HAADF-STEM images for $Au_{45}Pd_{55}/TiO_2$ nanoparticles (A), EDS mapping of $Au_{45}Pd_{55}/TiO_2$ (Au (blue) and Pd (red)) (B), and plot of Au composition in the as-synthesized AuPd nanoparticles (n in Au_nPd_{100-n} NPs, determined by ICP) *vs.* Au-precursor composition in the synthetic feeding composition (m in Au_mPd_{100-m} feeding). (C).

reflecting some differences in surface energy between Au atoms and Pd atoms.

In the following subsections, the *in situ* DRIFTS data for the nanoalloys under CO adsorption and oxidation conditions are first discussed to probe the surface catalytic sites of the nanoalloys with different compositions and upon different thermochemical treatments. Secondly, HE-XRD/PDF analysis was performed to assess the atomic-scale alloying and phase structures. In the last subsection, the surface structural data are discussed in correlation with the catalytic activities of CO oxidation in terms of the bimetallic composition and the thermochemical treatment parameters.

3.1. *In situ* DRIFTS characterization

DRIFTS was employed to probe the surface and catalytic sites over AuPd/TiO_2. The high sensitivity of CO stretching frequency to the binding sites on the nanoparticle surface allowed DRIFTS probing of the surface active sites of the thermochemically-treated AuPd/TiO_2 under two *in situ* conditions: (I) CO adsorption, and (II) CO + O_2 reaction, as schematically illustrated in Scheme 1.

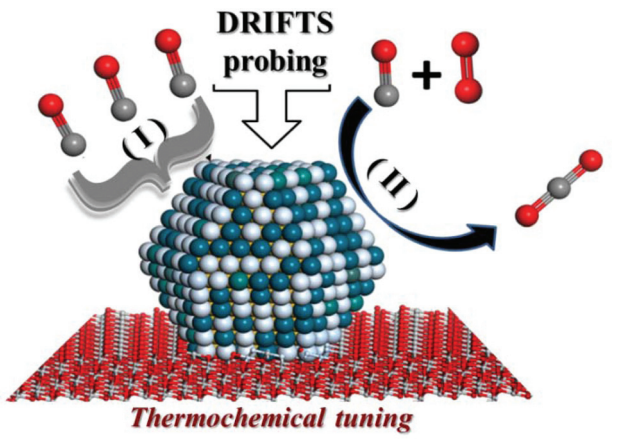

Scheme 1 Illustrations of *in situ* DRIFTs study of CO adsorption under CO only (I), and CO oxidation under CO + O_2 reaction condition (II) for different thermochemically-treated (under O_2 or H_2) AuPd/TiO_2 catalysts. Pd (cyan), Au (white), O (red), C (gray), and Ti (light gray).

The DRIFTs data of CO adsorption under CO only (I) are first examined. Fig. 2 shows a representative set of DRIFTs spectra to compare CO adsorption over $Au_{45}Pd_{55}/TiO_2$. Clearly, the spectral evolution and the peak position of CO adsorption peaks are highly dependent on the bimetallic composition under CO exposure (A) and under N_2 purge following the CO exposure (B). Upon CO exposure, there are two significant differences in terms of the CO peak evolution with time. First, the peak position depends strongly on the bimetallic composition. Major peaks in the range of ~2070–1800 cm^{-1} were clearly detected over $Au_{45}Pd_{55}$. According to earlier work,[35] the strongest CO peak at ~1955 cm^{-1} is assigned to CO on Pd bridge-site of the catalyst. There is a shoulder peak at ~1900 cm^{-1}, which is assigned to CO on Pd 3-fold site of the catalyst.

In the range of 2070–1800 cm^{-1}, weak peaks were observable over $Au_{45}Pd_{55}/TiO_2$ (Fig. 2A). These peaks were almost not detectable over $Au_{69}Pd_{31}/TiO_2$ (Fig. 3B). These results demonstrated that the surface adsorption sites were highly dependent on the bimetallic composition of the nanoalloys. For CO adsorption over $Au_{45}Pd_{55}/TiO_2$, the peak at ~2065 cm^{-1} is assigned to CO on Pd atop site. This peak does not seem to be associated with CO on Au atop site for two facts: (1) the control experiment with Au/TiO_2 shows the atop peak at a higher wavenumber (2090 cm^{-1}, see Fig. S6†); and (2) this peak did not show up with Au-rich $Au_{69}Pd_{31}/TiO_2$ (see Fig. 3B).

The wavenumbers of the observed three major peaks are all somewhat lower than those observed in previous studies, *e.g.*, peaks for linearly-adsorbed CO on Pd, bridge-bonded CO on Pd, and CO on Pd 3-fold sites at 2090, 1990, and 1930 cm^{-1}.[36] Overall, it appears that the bridge-site is dominant, indicating a relatively well-alloyed surface for $Au_{45}Pd_{55}/TiO_2$. The fact that on the Au-rich $Au_{69}Pd_{31}/TiO_2$ these peaks are essentially absent is suggestive of the lack of Pd–Pd bridge sites on the surface, and the adsorption on Au sites is apparently weakened by the presence of Pd likely underneath the surface Au layer.

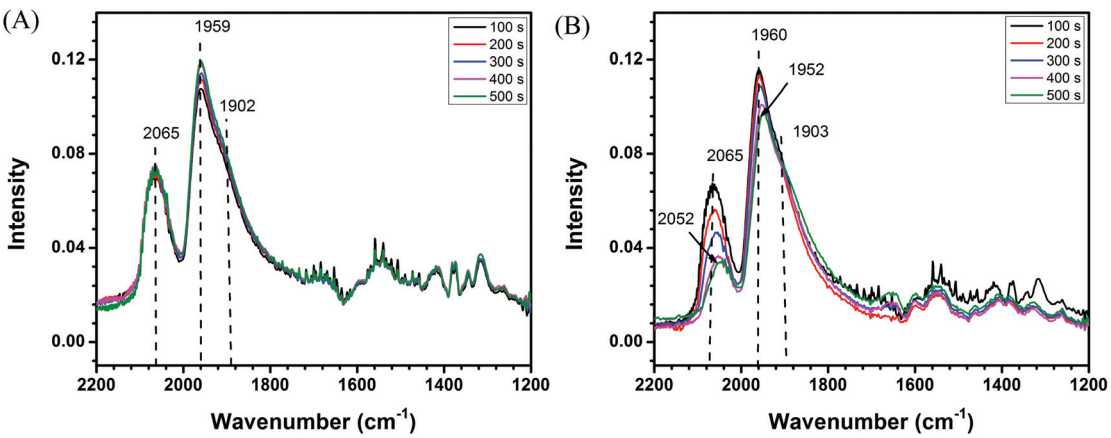

Fig. 2 *In situ* real-time DRIFTs spectral evolution of CO adsorption at room temperature over $Au_{45}Pd_{55}/TiO_2$. (A) Under CO exposure; (B) under N_2 purge following the CO exposure.

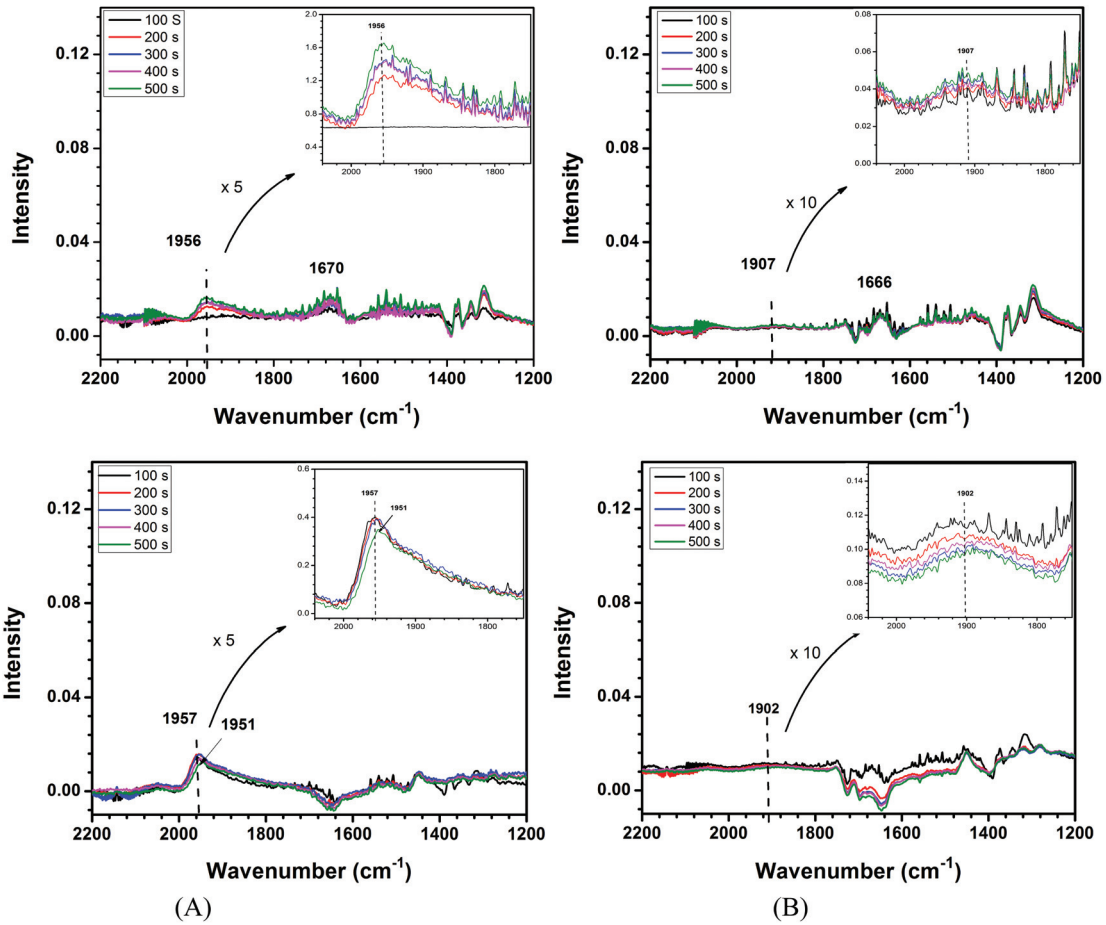

Fig. 3 *In situ* real-time DRIFTs spectral evolution of CO adsorption at room temperature over AuPd catalysts of different compositions: (A) Au_9Pd_{91}/TiO_2, and (B) $Au_{69}Pd_{31}/TiO_2$. Top panel: under CO exposure; Bottom panel: under N_2 purge following the CO exposure. Both spectra were corrected against the spectrum of gaseous CO exposed to pure support TiO_2.

However, for Pd-rich Au_9Pd_{91}/TiO_2, these peaks appeared weaker than $Au_{45}Pd_{55}/TiO_2$, which is not fully understood at this time. Note that there are some small negative peaks in the 1600–1700 cm^{-1} region, which were likely due to IR bands of uncorrected water residue in KBr used as background for the spectral correction. The catalyst in the compartment was purged with N_2 to remove the adsorbed water, but residue remained as evidenced by the broad negative band at about 3400 cm^{-1} (see Fig. S9†). The spectrum of TiO_2 was also used for the spectral correction, but the subtle difference between blank TiO_2 and catalyst-loaded TiO_2 did not enable an effective removal of the water bands (see Fig. S9†).

A close examination of the peaks at ~1956 and ~2065 cm^{-1} for Au_9Pd_{91} and $Au_{45}Pd_{55}/TiO_2$, *i.e.*, CO adsorbed on Pd atop and bridge sites, shows that the peak intensity was gradually increased with time (see Fig. 4A), along with a small shift toward a higher wavenumber. The intensity increase is indicative of an increased adsorption of CO, whereas the wavenumber shift reflects the dipole–dipole coupling effect as CO packing density is increased on the surface.[37] Upon N_2 purge following the CO exposure, the intensities of these CO peaks showed a gradual decrease and the peaks shift back to the lower wavenumbers (Fig. 4B). For $Au_{45}Pd_{55}/TiO_2$, in comparison with the increase of CO peak intensity at ~1959 cm^{-1} under CO exposure which appears faster than the peak at ~2065 cm^{-1}, the decrease of the CO peak at ~1959 cm^{-1} under N_2 purge appears slower. This kinetic difference is consistent with the difference in binding strength between the Pd atop and the Pd bridge sites.

Having analyzed the DRIFTs data of CO adsorption under CO only (I), we examined next the DRIFTs data under CO + O_2 reaction over $Au_{45}Pd_{55}/TiO_2$ subjected to two different thermochemical treatments. Under the reaction condition (CO + O_2) at different temperatures, the spectral feature of CO over the catalysts were shown to be highly dependent on the thermochemical treatment conditions. Fig. 5A shows a representative set of DRIFTs spectra under exposure to CO/O_2 at RT and 100 °C over $Au_{45}Pd_{55}/TiO_2$ after O_2 treatment at 260 °C for 30 minutes. Note that the spectra did not display the signature of oxygen species around (2035 to 2060 cm^{-1}) assigned to atop adsorption on Pd^{1+} and Pd^{2+},[38] indicative of the absence of Pd oxidation under CO + O_2 reactive environment. At RT (Fig. 5A-

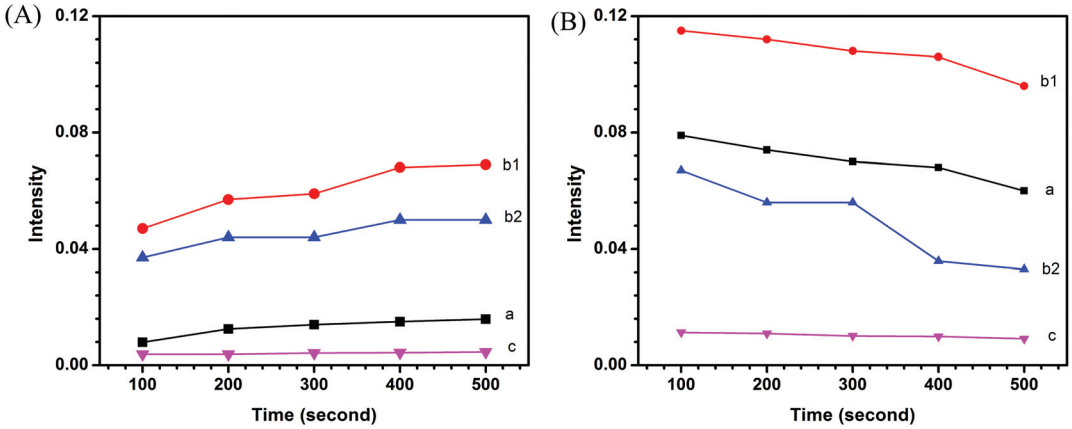

Fig. 4 Plots of peak intensity (absorbance peak height) *vs.* time for CO adsorption at room temperature over TiO_2-supported Au_9Pd_{91} (a, black, 1956 cm^{-1}), $Au_{45}Pd_{55}$ (b1, red, 1959 cm^{-1}; b2, blue, 2065 cm^{-1}), and $Au_{69}Pd_{31}$ (c, pink, 1907 cm^{-1}): under CO exposure (A); and under N_2 purge following the CO exposure (B). Au_9Pd_{91} (a, black, 1957 cm^{-1}), $Au_{45}Pd_{55}$ (b1, red, 1960 cm^{-1}; b2, blue, 2065 cm^{-1}), and $Au_{69}Pd_{31}$ (c, pink, 1902 cm^{-1}).

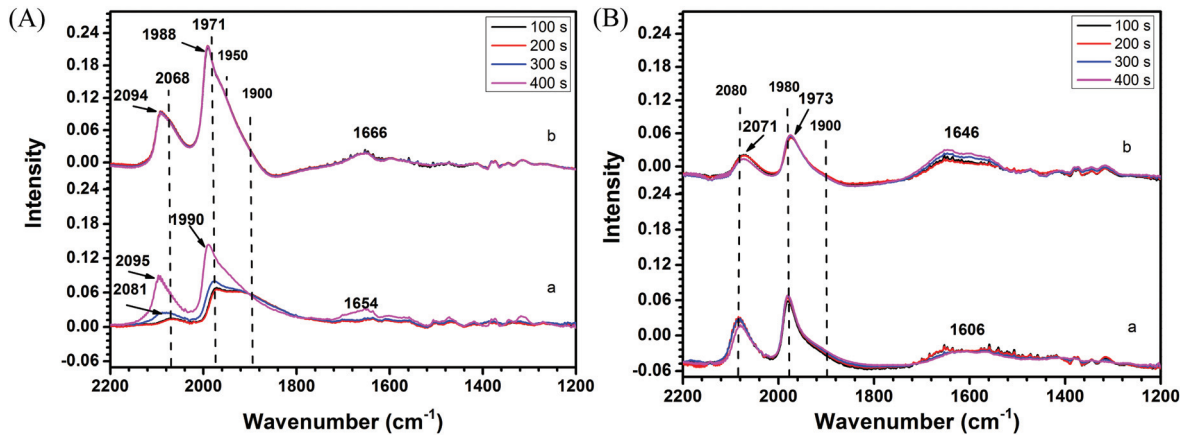

Fig. 5 *In situ* real-time DRIFTs spectral evolution collected under CO + O_2 reaction condition at different temperatures over $Au_{45}Pd_{55}/TiO_2$ catalyst after thermal treatment in O_2 at 260 °C for 30 min (A) and thermal treatment in H_2 at 400 °C for 30 min (B): at room temperature (a), and at 100 °C (b).

a), the peak at ~1971 cm^{-1} (CO on Pd bridge-site) showed an increase with reaction time, along with a subtle shift to a higher wavenumber. The peak at ~2068 cm^{-1} (CO on Pd atop site) showed a similar change. The shoulder peak at ~1900 cm^{-1} (CO three-fold hollow bonded)[39] appeared to remain unchanged. At higher temperatures, *e.g.*, 100 °C (Fig. 5A-b), the reaction time dependence of the spectra feature is clearly diminished, showing main peaks at ~2094, ~1988, and ~1950 cm^{-1} (shoulder), assigned to CO on atop and bridge sites. The peak intensities are higher than those at RT. The shoulder (~1900 cm^{-1}) virtually disappeared. After thermochemical treatment of the catalysts under H_2, the spectra at RT mainly feature the CO on Pd atop and bridge sites at ~2080 and ~1980 cm^{-1} (Fig. 5B-a). The shoulder peak at ~1900 cm^{-1} for CO on 3-fold site is much smaller. At 100 °C, the overall peak intensities are smaller than that at RT.

In contrast to the significant intensity increase for the O_2-treated catalyst by comparing the data between the 100 °C and room temperature (Fig. 6A-a), the peak intensities for the H_2-treated catalyst remain essentially unchanged over time (Fig. 6B-a). These peaks remain practically unchanged at higher temperature, *e.g.*, 100 °C, with a subtle shift to lower wavenumbers (~2071 and ~1973 cm^{-1}) (Fig. 5B-b). Interestingly, the broad peaks at ~1650 cm^{-1} showed an indication of increase in intensity over time (see Fig. 5B-b), likely reflecting the adsorbed intermediate (*e.g.*, carbonate species).

There are three major observations from the above DRIFTS data. First, the spectra for $Au_{45}Pd_{55}/TiO_2$ catalyst displayed stronger CO atop and bridge site peaks than those on the other two catalysts. Second, the spectra for H_2 treated $Au_{45}Pd_{55}/TiO_2$ showed time independence of the CO atop and bridge site peaks while revealing an increase of the product species, in contrast to the O_2 treated $Au_{45}Pd_{55}/TiO_2$. Third, in comparison with the strong peak intensities for the atop and bridge site peaks for the O_2 treated $Au_{45}Pd_{55}/TiO_2$, the peak intensities for the H_2 treated $Au_{45}Pd_{55}/TiO_2$ are much weaker. Moreover, the weaker peak intensities for the atop and bridge site peaks for the H_2 treated $Au_{45}Pd_{55}/TiO_2$ appear to be

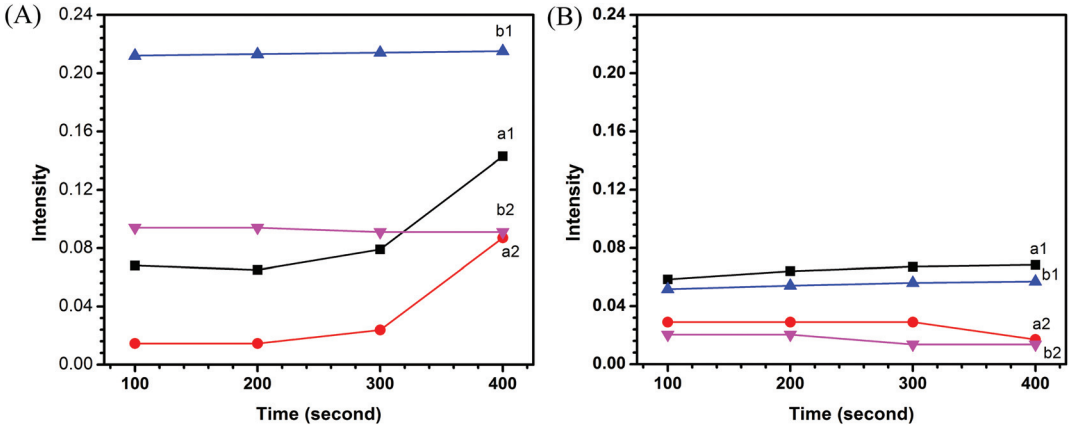

Fig. 6 Plots of peak intensity (absorbance peak height) *vs.* time under CO + O_2 reaction condition at different temperatures over $Au_{45}Pd_{55}/TiO_2$ catalyst after treatment under O_2 at 260 °C for 30 min (A) and treatment under H_2 at 400 °C for 30 min (B): at RT (a1-1971 cm^{-1}, a2-2061 cm^{-1}), and at 100 °C (b1-1980 cm^{-1}, b2-2080 cm^{-1}).

accompanied by a stronger peak intensity at ~1650 cm^{-1}. Importantly, a close comparison of the relative peak intensities for the main peak (~1970 cm^{-1}), corresponding to bridge sites, and the shoulder peaks at ~1900 cm^{-1}, corresponding to the 3-fold sites, was performed by spectral deconvolution (Table 1).

It is evident that the ratio of CO peak intensities of 3-fold *vs.* bridge site is greatly reduced by a factor of 2–3 after H_2 treatment comparing to that after O_2 treatment. The finding that the H_2 treated $Au_{45}Pd_{55}/TiO_2$ has much less 3-fold sites than that of the O_2 treated $Au_{45}Pd_{55}/TiO_2$ reflects a higher degree of alloying in the catalyst, which is consistent with HE-XRD/PDF data discussed next in this work and other different nanoalloys reported previously.[40] The thermochemical treatment promoted a reconstruction of the nanoalloy surface sites. For the treatment under oxygen, Pd is partially oxidized since it is more oxophilic than Au, which likely induces surface segregation and surface enrichment with Pd. Thus, the presence of electron-withdrawing species shifts the vibration frequency of the CO to a higher wavenumber. As will be discussed later, these observations are associated with the maximum activity of $Au_{45}Pd_{55}/TiO_2$ over the other compositions and the fact that H_2 treated $Au_{45}Pd_{55}/TiO_2$ is more active than the O_2 treated $Au_{45}Pd_{55}/TiO_2$. To further assess the surface active sites, the atomic-scale alloying and phase structures of the nanoalloys were further examined by HE-XRD coupled with PDF, as discussed next.

Table 1 Ratios of peak intensities of CO on 3-fold sites ($\nu(CO_{3\text{-fold}})$) *vs.* on bridge sites ($\nu(CO_{bridge})$) for $Au_{45}Pd_{55}/TiO_2$ based on spectral deconvolution (see Fig. S7 and S8 for details)

Treatment	Measurement	$I(\nu(CO_{3\text{-fold}})/I(\nu(CO_{bridge})$
O_2-Treated	Under CO + O_2 at RT	3.5
O_2-Treated	Under CO + O_2 at 100 °C	2.6
H_2-Treated	Under CO + O_2 at RT	1.2
H_2-Treated	Under CO + O_2 at 100 °C	1.1

3.2. Phase structures

Traditionally, synchrotron X-ray absorption spectroscopic techniques such as EXAFS (Extended X-ray Absorption Fine Structure) and XANES (X-ray Absorption Near Edge Structure) have been extensively used to study the atomic scale structures. As shown in our previous study,[25] XANES/EXAFS was used to determine the local atomic coordination structure and metal surface oxygenated species of nanoalloys of binary and ternary compositions. However, these techniques are limited in terms of providing information about chemical ordering, structural deformation/strain and phase properties, which can, however, be assessed by HE-XRD coupled with PDF analysis,[34] a powerful technique for determining the atomic-scale phase structure of nanoparticles.[41] In this work, we used HE-XRD/PDF to analyze the atomic-scale phase structures of the nanoalloys. Fig. 7A shows a representative set of PDFs for thermochemically-treated $AuPd/TiO_2$ with three different compositions, which were derived from the HE-XRD data. The PDFs show a sequence of sharp peaks, indicating the existence of well-defined atomic coordination spheres in the NPs. The results show that the nanoparticles possess atomic arrangement similar to the face-centered cubic (fcc) structure. The fcc-model fitted lattice parameter (α) provides an approximation of the interatomic distances in the nanoalloys. The PDFs are well fitted with fcc structure with the lattice constant showing an increase with increasing Au% in the NPs (α = 3.969 Å to 3.832 Å for n = 45 to 69). In comparison, the PDFs for both as-synthesized and thermochemically-treated AuPd NPs supported on carbon with different compositions also show an increase with increasing Au% in the NPs, but lattice parameter being greater than those for the $AuPd/TiO_2$ samples (*e.g.*, α = 4.003 Å to 4.009 Å for n = 45 to 69 in the NPs, and α = 3.997 Å to 4.012 Å for n = 45 to 69 in the NPs/C) (Fig. S2†). It is evident that the experimental PDFs for the AuPd nanoparticles exhibit physical oscillations *vs.* real space distances close to the size of the respective nanoparticle (~6.3 nm). This is indicative of structural distortion, which is common in nanoparticles due

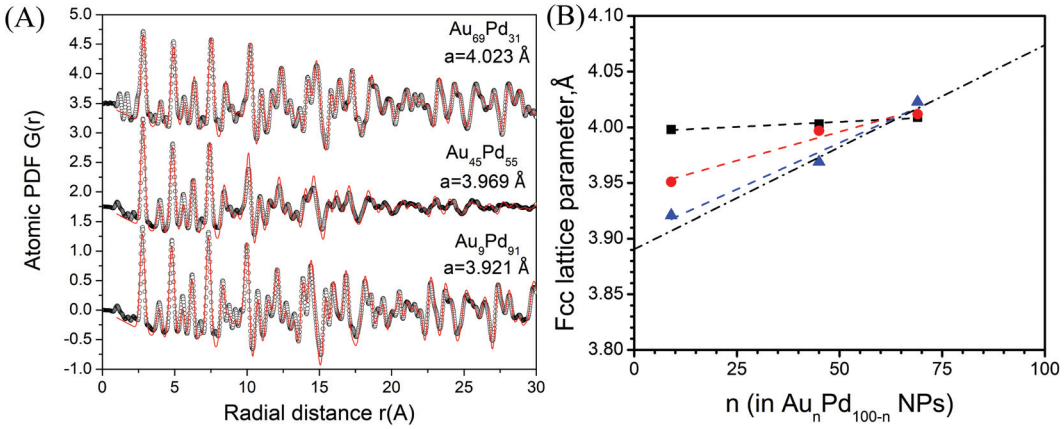

Fig. 7 Experimental (symbols in black) and model (line in red) total atomic PDFs for thermochemically-treated AuPd/TiO_2 with three different compositions (A), and plots of fcc-lattice parameter of as-synthesized AuPd/C NPs (symbols in black) and thermochemically-processed AuPd/C (symbols in red) (treated/(N_2 + H_2) and AuPd/TiO_2) (symbols in blue) as a function of the relative Au content in the NPs. Broken (dash dot) line represents a 1 : 1 relationship.

to finite size and surface relaxation effect. This structural disorder varies based on the synthesis process and the thermochemical treatment. It also affects physicochemical property of NPs.[19] Thermochemical treatment in reactive gas environment has significant effect on atomic structure, causing reduction and expansion of lattice parameters.[42]

The so-called lattice parameters of AuPd nanoalloy extracted from the experimental PDF data are summarized in Fig. 7B. For the as-synthesized NPs, the lattice parameter increases with increasing Au% in an approximately linear fashion. However, the slope (1.8×10^{-4}) is much smaller than that according to Vegard's law (1.8×10^{-3}-dotted line). The situation is different for the supported nanoparticles after the thermochemical treatment, where the slope for AuPd/C (1.0×10^{-3}) and that for AuPd/TiO_2 (1.67×10^{-3}) are clearly increased, approaching that predicted by Vegard's law. This finding suggests that the as-synthesized AuPd nanoparticles were under very extensive tensile stress.[43] This is common in nanoparticle due to change in electronic structure of alloy as result of charge transfer between the two components. Note that pure Au NPs exhibit a compressive stress,[34] which is consistent with lattice shrinking for Au-rich AuPd NPs. However, the thermochemical treatment of the nanoparticles and the type of the support appears to relief a significant part of the tensile stress or result in redistribution of Au and Pd atoms in the particle.

An important finding is that the degree of alloying and the interatomic distance depend strongly on the nanoalloy–support interaction. As stated, the fcc-type lattice parameter provides an approximation of overall interatomic bonding distances. The decreased bonding distances for AuPd/TiO_2 in comparison with AuPd/C is attributed to redistribution of charge between Au and Pd atoms as a result of different nanoalloy–support interactions, including minimization of local strain. That is, larger Au atom "shrinks" whereas smaller Pd atom "expands" so that the ratio of their atomic size becomes as close to one as possible for minimization of local tensile strain. Based on the results in this work, we believe that it is the strong nanoalloy–TiO_2 interaction that led to a further relief of the tensile stress in the NPs, at which the phase structure can be characterized as a random alloy. The comparison of the atomic structures between as-synthesized and thermochemically-treated catalysts supported on carbon were studied in this work and in our previous work,[34] in which the interference of inert carbon support to diffraction pattern was insignificant. However, in the case of TiO_2 support, the thermochemical treatment could reduce TiO_2, leading to a significant relief of lattice strain. Based on the comparison of the carbon-supported AuPd NPs between as-synthesized and thermochemically-treated states (see Fig. 7B), we believe inhomogeneity was insignificant for the as-synthesized AuPd/C. The HE-XRD/PDF analysis revealed an enhanced degree of random alloying. This type of structural characteristics reflected the intrinsic properties of fresh catalysts in correlation with their catalytic activities, which was used a structural descriptor of the nanoscale alloying in assessing the catalytic activity of CO oxidation in correlation with surface binding sites, as discussed next.

3.3. Structural correlation with catalytic activity

The temperature dependence of the catalytic oxidation of CO over C and TiO_2 supported AuPd nanoalloys and those after thermochemical treatment was examined (Fig. S3†). The thermochemical treatment was performed at 260 °C under O_2 followed by H_2 at 400 °C. The catalyst was exposed to air before being loaded into the catalyst test bed, and were further treated under H_2 or O_2 before the catalytic activity measurements. For CO conversion over carbon-supported Au_9Pd_{91}, $Au_{45}Pd_{55}$, and $Au_{69}Pd_{31}$/C catalysts, the catalyst with Au : Pd ~ 50 : 50 (*i.e.*, $Au_{45}Pd_{55}$) is shown to display a higher activity than that with Au : Pd > 50 : 50 (*i.e.*, $Au_{69}Pd_{31}$), as evidenced by the composition dependence of the catalytic activity in terms of

the reaction temperature (Fig. S3†). The catalytic activity of AuPd/C catalysts showed little difference after thermochemical treatments in the oxidative and reductive reaction atmospheres, reflecting the inert properties of gold and palladium. In sharp contrast, the activity of AuPd NPs supported on TiO_2 measured under the same condition exhibit significant differences (Fig. S4†) shows a clear dependence on the thermochemical treatment atmosphere, displaying an increase in the order of H_2-treated (blue) > O_2-treated (red) > freshly-prepared catalysts (black) in terms of the reaction temperature.

By a comparison of the reaction temperatures at which 50% CO conversion was achieved, *i.e.*, T_{50} values, for CO oxidation over AuPd/C and AuPd/TiO_2 catalysts (Fig. 8A and B), the T_{50} value was observed to increase with Au% in the AuPd/C catalysts, exhibiting an observable minimum at a composition of ~50% Au. This trend is practically independent on the thermochemical treatment atmosphere. In contrast, the T_{50} value for AuPd/TiO_2 catalysts was found to exhibit a clear minimum at a composition of 50% Au (Fig. 8B). This activity-composition relationship showed a strong dependence on the thermochemical treatment atmosphere. The O_2-treated catalyst showed the most significant change in terms of composition dependence which was followed by the H_2-treated catalyst, in comparison with the as-prepared catalysts. The sharp contrast between AuPd/C and AuPd/TiO_2 catalysts is believed to reflect the differences in active sites for oxygen activation as a result of the nanoalloy–support interaction,[44] in addition to the perimeter zone effect between nanoalloys and TiO_2.

The catalytic data were further analyzed to assess the reaction kinetics in terms of the apparent activation energy (E_a) over the AuPd catalysts on two different supports (Table 2). Values of E_a were obtained from Arrhenius plot (Fig. S5†). For CO oxidation over AuPd/C catalysts (Table S1†), the apparent activation energy is shown to decrease with increasing gold in the bimetallic nanoparticles. For the catalyst with Au : Pd < 50, E_a is increased after H_2 treatment in comparison with that after O_2 treatment. For example, E_a for Au_9Pd_{91} was 207 kJ mol^{-1} after H_2 treatment and 204 kJ mol^{-1} after O_2 treatment. E_a for $Au_{45}Pd_{55}$ was 195 kJ mol^{-1} after H_2 treatment and 94 kJ mol^{-1} after O_2 treatment. In comparison with data obtained in our previous studies for CO oxidation over PdCu catalysts,[45] the E_a values are slightly larger. In comparison, the activation energy for CO oxidation over AuPd/TiO_2 catalysts (Table S1†) showed a significant reduction and less–significant dependence on the composition. For example, the observed apparent activation energies for $Au_{45}Pd_{55}/TiO_2$ and $Au_{69}Pd_{31}/TiO_2$ were 34 kJ mol^{-1}, and 58 kJ mol^{-1} after O_2 treatment, and 6 kJ mol^{-1}, and 32 kJ mol^{-1}, respectively, after H_2 treatment.

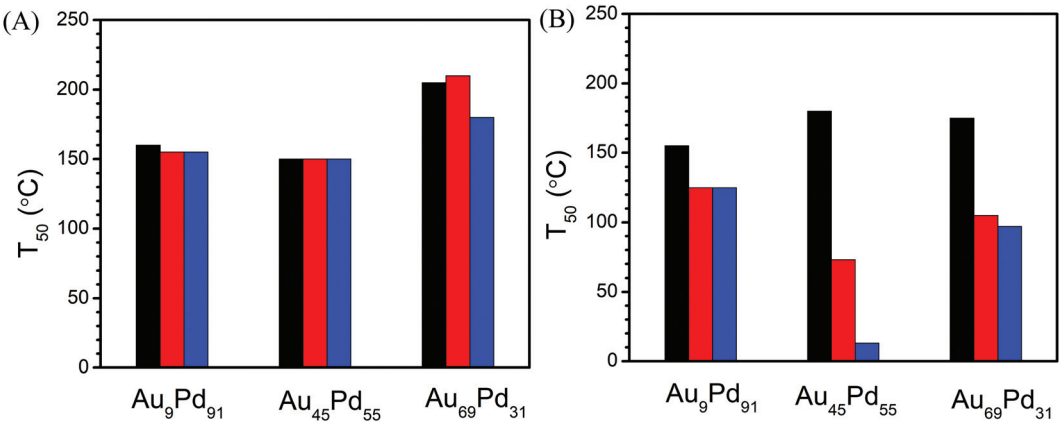

Fig. 8 Plots of T_{50} values for CO oxidation over AuPd/C (A) and AuPd/TiO_2 (B) for fresh catalysts (black), catalysts treated under O_2 at 260 °C for 30 min (red), and catalysts treated under H_2 at 400 °C for 30 min (blue). (Standard deviation of the reaction temperature: ±1.8 °C.)

Table 2 DFT-calculated adsorption energy (eV) for molecularly adsorbed CO on Au_nPd_{13-n} clusters (n = 0, 1, 6, 9, and 13). Pd (cyan), Au (white), carbon (gray), and oxygen (red)

Pd_{13}	Au_1Pd_{12}	Au_6Pd_7	Au_9Pd_4	Au_{13}
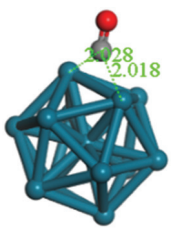	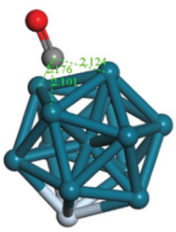	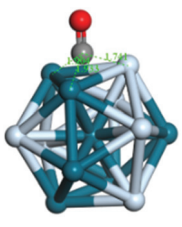	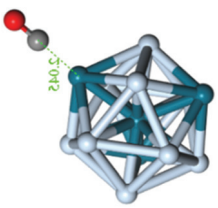	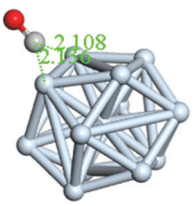
2.13	2.19	1.92	1.74	0.96

These values are quite close to those for CO oxidation over PdNi catalysts.[24]

The T_{50} for AuPd/TiO_2 catalysts of different compositions (Fig. 8A and B) appeared to be highly dependent on the thermochemical treatment conditions whereas T_{50} for AuPd/C catalysts was not. Based on the estimated activation energy (E_a, Table S1†), the values of E_a for AuPd/TiO_2 catalysts were also found to be relatively insensitive to the thermochemical treatment conditions. As suggested by HE-XRD/PDF results discussed earlier, the formation of random alloy in NPs/TiO_2 as a result of the strong nanoalloy–support interaction is likely a key factor contributing to the surface sites responsible for the higher catalytic activity for CO oxidation over AuPd/TiO_2 catalysts than over AuPd/C. Note that the reaction rate was previously shown to be largely independent of the metal loading on the catalyst when being tested with various dilutions of metal loading for different nanoalloy catalysts (<5%).[25] The finding could rule out temperature and concentration gradient induced diffusional mass transport effect on the kinetic assessment. However, for the catalysts studied in this work which had a metal loading of 15% in order for enhancing the signals in HE-XRD measurement, the apparent activation energy may partially reflect some contribution from mass transport, which is yet to be confirmed in future work. While the HE-XRD/PDF data were collected under *ex situ* condition, it reveals differences in the alloy structures of different compositions, which provides important information to aid the assessment of the structural correlation of the catalytic activity, as supported by our previous studies of different nanoalloy catalysts under both *ex situ* and *in situ* conditions.[23,24]

In our recent 3D modeling studies of the composition-structure correlation in terms of the coordination numbers and the distribution of surface Au–Au, Pd–Pd, and Pd–Au bonding distances on the nanoparticle surface for AuPd/C,[34] in relation to the PDFs shown in Fig. S2,† it was shown that the degree of alloying is maximized on the nanoparticle surface, as reflected by the maximized Au–Pd and Pd–Au atomic pairs. As a result, Au atoms shrink whereas Pd atoms expand, indicating that Pd and Au atoms are under tensile and compressive stresses due to the mismatch between the size Au and Pd atoms which in bulk state is 2.872 and 2.75 Å respectively. Since a tensile stress is considered for the surface atoms on the NP, which shifts d-band energy (ε_d) up toward Fermi level, a stronger metal–adsorbate is expected, and *vice versa*. By analyzing the total surface coordination number (CN) derived from the 3D modeling[34] which reflects the degree of alloying in terms of surface sites, as shown in Fig. 9, the total surface CNs in terms of all surface partial CNs of the first-neighboring Au–Au (Fig. 9A), Pd–Pd (Fig. 9B) and Pd–Au (Fig. 9C) pairs are shown to depend on the bimetallic composition differently for the different pairs. While the total surface CNs for Pd–Pd show a minimum at ~50 Au%, the total surface CNs for both Au–Au and Pd–Au exhibit maxima at ~50 Au% (Fig. 9). It is thus the alloyed site, along with domains of Au atoms, on the surface for the catalyst with Au : Pd ~ 50 that is responsible for the maximized catalytic activity of CO oxidation. On such surface, the activation of CO or O_2 adsorbed on the site of Pd surrounded by Au atoms is more favored than other surface sites, in which the Au atoms may also aid the maneuvering of reaction intermediates.

The different nanoalloy–support interactions in different nanoalloy catalysts[23,25] could also influence the tensile stress. For AuPd/TiO_2, fcc-type lattice structure seems to show an enhanced relief of the tensile stress towards random alloy character in comparison with AuPd/C. It is interesting that at Au% ~ 50 the decrease of Pd–Pd CNs is accompanied by maximization of Au–Au CNs, during which the average surface Pd–Au first coordination number is maximized. For AuPd/C, the formation of a random alloy at a composition of $n \sim 50$ would favor the maximization of Pd–Au first CN. For CO oxidation, the composition-dependent catalytic synergy (Fig. 8) is believed to be linked to the overall surface CNs. For TiO_2-supported AuPd NPs, a similar trend in the surface coordination number *vs.* bimetallic composition is possible, but the interaction between the nanoalloy and the high-oxygen capacity TiO_2 support could lead to a subtle difference in comparison with the nanoalloy–carbon support interaction. TiO_2 has strong interaction with AuPd nanoparticle,[46] which contributes to a more significant reduction of interatomic distances. As a result of the consequent random alloy character, the activity for AuPd/TiO_2 is higher than AuPd/C. In addition, TiO_2 support provides oxygen-activation sites through oxygen

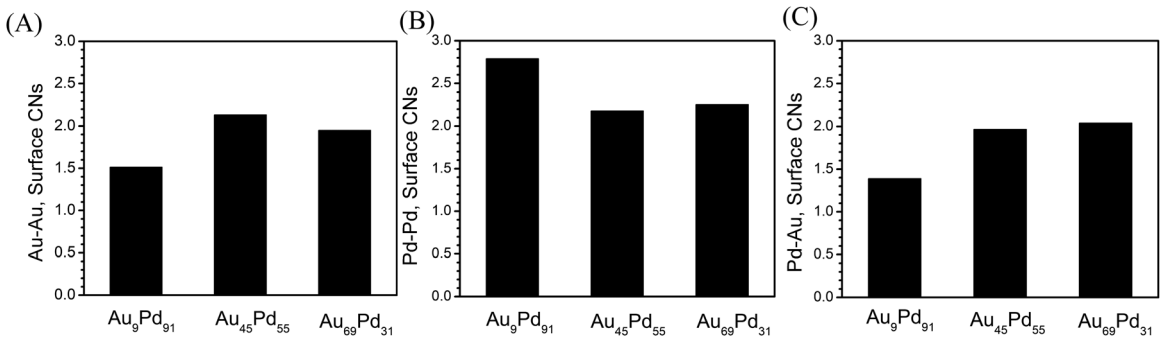

Fig. 9 Plots of average total surface CNs in terms of all surface partial CNs of the first-neighboring Au–Au (A), Pd–Pd (B) and Pd–Au (C) pairs for AuPd/C catalysts with different bimetallic compositions. Data were extracted from the data in Fig. 5 (left graph) presented in ref. 32.

Scheme 2 Illustration of the difference of surface binding sites for CO adsorption on the surface of alloyed $Au_{50}Pd_{50}$ surface between O_2 (A) and H_2 (B) treated AuPd nanoalloys supported on TiO_2. Pd (green), Au (light blue).

deficiency sites located at the nanoalloy–support perimeter zone,[25] different from active sites on the nanoparticle surface. The catalytic oxidation of CO at low temperatures proceeds through Langmuir–Hinshelwood mechanism including adsorbed CO and O atoms.[47] The adsorption of CO and dissociative chemisorption of oxygen are the main two factors that influence the catalytic performance.[48] The increase of Au% on nanoparticle surface would lead to isolation of Pd by Au (ensemble effect)[49] resulting in prevention of active sites from poisoning. Since Au has higher electronegativity (2.5) than Pd (2.2), charge transfer occurs from Pd to Au (ligand effect), facilitating the adsorption of reactants[50] by shifting the d-band center away from Fermi level and in turn it leads to a weaker interaction between adsorbates and Pd surface.[51]

The significance of these factors substantiates the assessment of the fact that the maximization of CO atop and bridge sites for the catalyst at Au : Pd atomic ratio of ~50 : 50 coincides with the maximization of the alloying degree when Au% ~ 50. Scheme 2 depicts CO adsorption on the surfaces of O_2 and H_2 treated $Au_{45}Pd_{55}/TiO_2$. Note that the surface metal atoms remain in the reduced state in both cases. In comparison with the presence of atop, bridge and 3-fold sites on the surface for the O_2-treated $Au_{45}Pd_{55}/TiO_2$, the H_2-treated $Au_{45}Pd_{55}/TiO_2$ feature largely atop and bridge sites as a result of a higher degree of alloying on the surface.

The catalytic synergy is also supported by consideration of the CO adsorption energy based on preliminary DFT calculation results using small AuPd clusters. For adsorption of CO on the surfaces of a 13-atom cluster model of AuPd, the adsorption energy of CO was obtained by DFT calculation on the basis of Yeager model. The results are shown in Table 2, showing a decrease of adsorption energy with the Au% increase.

There appears to be a maximum of adsorption energy at Au_1Pd_{12}. It is interesting that the adsorption energy of CO on Au_6Pd_7 falls in between Au_1Pd_{12} and Au_9Pd_4 The adsorption site features 3-fold Pd site for Au_1Pd_{12} and 3-fold Pd–Pd–Au site for Au_6Pd_7, and atop Pd site for Au_9Pd_4. In correlation with the experimentally-observed maximum activity for the catalysts with Au : Pd ~ 50, the intermediate adsorption energy and the participation of Au atom in the adsorption site for CO seem to be important factors for further probing the catalytic synergy. It is important to note that the DFT result was based on a small cluster model. Further work is needed for an in-depth assessment. As a preliminary assessment, DFT calculations of the adsorption energy of CO on a AuPd surface (111) model (modeling larger-sized particles) were also performed (Table S2†). The result revealed a similar trend for the adsorption energy with a subtle shift of the maximum to Au_6Pd_7 (Table S2†), which coincided with the maximum activity observed for $Au_{45}Pd_{55}$. In addition, the adsorption energy for CO adsorption on a 3-fold hollow Pd site was found to be greater than that on a bridge or atop Pd site (see Table S2†), which also qualitatively agreed with the experimental data. A detailed understanding the calculation results is part of our on-going investigations.

4. Conclusions

In conclusion, the thermochemically-induced reconstruction of the surface active sites on Ti_2O-supported AuPd nanoalloys was probed by *in situ* DRIFTS, revealing enrichment of bridge and atop Pd sites under hydrogen, in contrast to enrichment of three-fold hollow sites under oxygen. This surface evolution is shown to be highly dependent on the bimetallic composition and the support–nanoalloys interaction. The relief of a significant part of the tensile stress in the nanoalloys, as supported by HE-XRD/PDF analysis of nanoalloys phase and interatomic bonding structures in the nanoalloys, was believed to play an important role in the nanoscale reconstruction, leading to a random distribution of Au and Pd atoms in the nanoparticles. The nanoscale alloying and surface site evolution characteristics were found to correlate strongly with the catalytic activity of CO oxidation in terms of the bimetallic composition and thermochemical treatment condition, revealing a composition-dependent catalytic synergy. These findings have demonstrated an important pathway for fine-tuning the surface catalytic sites of nanoalloys catalysts, which have significant implications for advancing the design of nanoalloys-based catalysts with the desired catalytic synergy.

Author contribution

Haval Kareem carried out the catalyst preparation, the catalyst characterization, and the activity measurement, and participated in the data analysis and the manuscript writing. Shiyao Shan participated in the design of the catalytic measurement, the catalyst preparation and characterization, the data analysis, and the manuscript writing. Fang Lin participated in the catalyst characterization and the activity measurement. Jing Li participated in the data analysis. Zhipeng Wu performed DFT calculation and participated in the data analysis. Binay Prasai participated in the HE-XRD measurement and the PDF data analysis. Casey O'Brien carried out the *in situ* DRIFT measurement, and participated in the data analysis and the manuscript writing. Ivan Lee designed and coordinated the *in situ* DRIFT measurement, and participated in the data analysis and the manuscript writing. Dat T. Tran participated in the *in situ* DRIFT measurement and the data analysis. Lefu Yang participated in the design of the catalytic measurement and the data analysis. Derrick Mott contributed to the STEM measurement and data analysis. Jin Luo participated in the catalyst characterization and the manuscript writing. Valeri Petkov designed the HE-XRD study, performed the HE-XRD measurement and PDF analysis, and participated in the manuscript writing, Chuan-Jian Zhong designed the study, coordinated the experimental measurements and the data analysis, and participated in the manuscript writing and revisions.

Conflicts of interest

There are no conflicts to declare.

Acknowledgements

This work was supported by the National Science Foundation (CHE 1566283) and the Department of Energy - Basic Energy Sciences (DE-SC0006877). Work at the Advanced Photon Source was supported by DOE under Contract DE-AC02-06CH11357. Thanks are also due to 1-ID beamline staff for the help with the HE-XRD experiment.

References

1 World Health Organization, *Carbon monoxide, Environmental Health Criteria 213*, World Health Organization, Geneva, 1999.
2 Y. Yang, K. M. Saoud, V. Abdelsayed, G. Glaspell, S. Deevi and M. S. El-Shall, *Catal. Commun.*, 2006, **7**, 281.
3 T. Schmidt, Z. Jusys, H. Gasteiger, R. Behm, U. Endruschat and H. Boennemann, *J. Electroanal. Chem.*, 2001, **501**, 132.
4 J. Zhang and A. N. Alexandrova, *J. Phys. Chem. Lett.*, 2013, **4**, 2250.
5 M. Mougenot, A. Caillard, M. Simoes, S. Baranton, C. Coutanceau and P. Brault, *Appl. Catal., B*, 2011, **107**, 372.
6 C.-W. Yi, K. Luo, T. Wei and D. Goodman, *J. Phys. Chem. B*, 2005, **109**, 18535.
7 A. Hungría, N. Browning, R. Erni, M. Fernández-García, J. Conesa, J. Pérez-Omil and A. Martínez-Arias, *J. Catal.*, 2005, **235**, 251.
8 J. K. Edwards, B. E. Solsona, P. Landon, A. F. Carley, A. Herzing, C. J. Kiely and G. J. Hutchings, *J. Catal.*, 2005, **236**, 69.
9 E. Allison and G. Bond, *Catal. Rev.*, 1972, **7**, 233.
10 V. Petkov, B. Prasai, Y. Ren, S. Shan, J. Luo, P. Joseph and C. J. Zhong, *Nanoscale*, 2014, **6**, 10048.
11 C. M. Olmos, L. E. Chinchilla, J. J. Delgado, A. B. Hungría, G. Blanco, J. J. Calvino and X. Chen, *Catal. Lett.*, 2016, **146**, 144.
12 R. W. Scott, C. Sivadinarayana, O. M. Wilson, Z. Yan, D. W. Goodman and R. M. Crooks, *J. Am. Chem. Soc.*, 2005, **127**, 1380.
13 M. B. Griffin, A. A. Rodriguez, M. M. Montemore, J. R. Monnier, C. T. Williams and J. W. Medlin, *J. Catal.*, 2013, **307**, 111.
14 J. Rebelli, M. Detwiler, S. Ma, C. T. Williams and J. R. Monnier, *J. Catal.*, 2010, **270**, 224.
15 A. Venezia, L. Liotta, G. Pantaleo, V. La Parola, G. Deganello, A. Beck, Z. Koppány, K. Frey, D. Horvath and L. Guczi, *Appl. Catal., A*, 2003, **251**, 359.
16 D. Cheng, H. Xu and A. Fortunelli, *J. Catal.*, 2014, **314**, 47.
17 A. Jabloński, S. Overbury and G. Somorjai, *Surf. Sci.*, 1977, **65**, 578.
18 C. P. O'Brien and I. C. Lee, *J. Catal.*, 2017, **347**, 1.
19 F. Gao and D. W. Goodman, *Chem. Soc. Rev.*, 2012, **41**, 8009.
20 M. Chen, D. Kumar, C.-W. Yi and D. W. Goodman, *Science*, 2005, **310**, 291.
21 L. Delannoy, S. Giorgio, J. G. Mattei, C. R. Henry, N. El Kolli, C. Méthivier and C. Louis, *ChemCatChem*, 2013, **5**, 2707.
22 B. Zhu, G. Thrimurthulu, L. Delannoy, C. Louis, C. Mottet, J. Creuze, B. Legrand and H. Guesmi, *J. Catal.*, 2013, **308**, 272–281.
23 S. Shan, V. Petkov, L. Yang, D. Mott, B. N. Wanjala, F. Cai, B. H. Chen, J. Luo and C. J. Zhong, *ACS Catal.*, 2013, **3**, 3075.
24 S. Shan, V. Petkov, L. Yang, J. Luo, P. Joseph, D. Mayzel, B. Prasai, L. Wang, M. Engelhard and C. J. Zhong, *J. Am. Chem. Soc.*, 2014, **136**, 7140.
25 L. Yang, S. Shan, R. Loukrakpam, V. Petkov, Y. Ren, B. N. Wanjala, M. H. Engelhard, J. Luo, J. Yin and Y. Chen, *J. Am. Chem. Soc.*, 2012, **134**, 15048–15060.
26 Ö. Metin, X. Sun and S. Sun, *Nanoscale*, 2013, **5**, 910.
27 R. Loukrakpam, J. Luo, T. He, Y. Chen, Z. Xu, P. N. Njoki, B. N. Wanjala, B. Fang, D. Mott and J. Yin, *J. Phys. Chem. C*, 2011, **115**, 1682.
28 S. M. Oxford, P. L. Lee, P. J. Chupas, K. W. Chapman, M. C. Kung and H. H. Kung, *J. Phys. Chem. C*, 2010, **114**, 17085.
29 T. Egami and S. J. L. Billinge, *Underneath the Braggs' Peak*, Pergamon, Amsterdam, Netherlands, 2003.

30 D. Wang, A. Villa, F. Porta, L. Prati and D. Su, *J. Phys. Chem. C*, 2008, **112**, 8617.
31 A. R. Denton and N. W. Ashcroft, *Phys. Rev. A*, 1991, **43**, 3161.
32 P. Paalanen, B. M. Weckhuysen and M. Sankar, *Catal. Sci. Technol.*, 2013, **3**, 2869–2880.
33 J. Pritchard, L. Kesavan, M. Piccinini, Q. He, R. Tiruvalam, N. Dimitratos, J. A. Lopez-Sanchez, A. F. Carley, J. K. Edwards and C. J. Kiely, *Langmuir*, 2010, **26**, 16568–16577.
34 V. Petkov, B. Prasai, S. Shastri, J.-W. Kim, S. Shan, H. R. Kareem, J. Luo and C. J. Zhong, *J. Phys. Chem. C*, 2017, **121**, 7854.
35 C. Lentz, S. P. Jand, J. Melke, C. Roth and P. Kaghazchi, *J. Mol. Catal. A: Chem.*, 2017, **426**, 1.
36 B. Zhu, G. Thrimurthulu, L. Delannoy, C. Louis, C. Mottet, J. Creuze, B. Legrand and H. Guesmi, *J. Catal.*, 2013, **308**, 272–281.
37 E. K. Gibson, A. M. Beale, C. R. A. Catlow, A. Chutia, D. Gianolio, A. Gould, A. Kroner, K. M. Mohammed, M. Perdjon and S. M. Rogers, *Chem. Mater.*, 2015, **27**, 3714.
38 J. B. Giorgi, T. Schroeder, M. Bäumer and H.-J. Freund, *Surf. Sci.*, 2002, **498**, 71–77.
39 X. Xu and D. W. Goodman, *J. Phys. Chem.*, 1993, **97**, 7711.
40 I. Jbir, A. Paredes-Nunez, S. Khaddar-Zine, Z. Ksibir, F. Meunier and D. Bianchi, *Appl. Catal., A*, 2015, **505**, 309.
41 C.-W. Yi, K. Luo, T. Wei and D. Goodman, *J. Phys. Chem. B*, 2005, **109**, 18535–18540.
42 F. Liu, D. Wechsler and P. Zhang, *Chem. Phys. Lett.*, 2008, **461**, 254.
43 V. Petkov, S. Shan, P. Chupas, J. Yin, L. Yang, J. Luo and C. J. Zhong, *Nanoscale*, 2013, **5**, 7379.
44 B. D. Mukri, G. Dutta, U. V. Waghmare and M. Hegde, *Chem. Mater.*, 2012, **24**, 4491–4502.
45 S. Shan, V. Petkov, B. Prasai, J. Wu, P. Joseph, Z. Skeete, E. Kim, D. Mott, O. Malis and J. Luo, *Nanoscale*, 2015, **7**, 18936.
46 V. Mukundan, J. Yin, P. Joseph, J. Luo, S. Shan, D. N. Zakharov, C. J. Zhong and O. Malis, *Sci. Technol. Adv. Mater.*, 2014, **15**, 025002.
47 P. J. Berlowitz, C. H. Peden and D. W. Goodman, *J. Phys. Chem.*, 1988, **92**, 5213.
48 H. Conrad, G. Ertl and J. Küppers, *Surf. Sci.*, 1978, **76**, 323.
49 F. Besenbacher, I. Chorkendorff, B. Clausen, B. Hammer, A. Molenbroek, J. K. Nørskov and I. Stensgaard, *Science*, 1998, **279**, 1913.
50 F. Maroun, F. Ozanam, O. Magnussen and R. Behm, *Science*, 2001, **293**, 1811.
51 L. Guczi, A. Beck, A. Horvath, Z. Koppány, G. Stefler, K. Frey, I. Sajo, O. Geszti, D. Bazin and J. Lynch, *J. Mol. Catal. A: Chem.*, 2003, **204**, 545.

